2024 IEEE International Symposium on Biomedical Imaging (ISBI) | 979-8-3503-1333-8/24/$31.00 ©2024 IEEE | DOI: 10.1109/ISBI56570.2024.10635547

A MOMENT-BASED WEIGHTED BLOCK SPARSE BAYESIAN LEARNING APPROACH FOR SIMULTANEOUS DUAL-LAYER LUNG ELECTRICAL IMPEDANCE TOMOGRAPHY

Christos Dimas, Vassilis Alimisis, Nikolaos Uzunoglu and Paul P. Sotiriadis

National Technical University of Athens

ABSTRACT

Electrical impedance tomography (EIT) has emerged as a non-invasive, fast, and safe medical technique for real-time thoracic imaging. However, EIT is typically conducted in a 2D fashion, often lacking crucial structural information associated with the z-axis direction. Furthermore, 3D EIT incurs high computational costs, rendering it impractical for real-time monitoring, while EIT reconstruction is an ill-posed and nonlinear problem. In this paper, a weighted block sparse Bayesian learning and an efficient method-of-moment approach are combined to simultaneously conduct lung EIT in 2 distinct z-planes, each one defined by 16 electrodes. Therefore, the inverse problem's non-linearity is reduced, robustness to noise and modeling errors is improved, while z-axis information is obtained, avoiding the 3D case complexity. Reconstructions based on simulated human thoracic structures and on horse subject thoracic data demonstrate improvement spatial resolution with limited presence of artefacts compared to the linear method-of-moment reconstruction.

***Index Terms*—** Electrical impedance tomography, lung, moment, sparse Bayesian learning, electrode layer.

1. INTRODUCTION

Electrical impedance tomography (EIT) is an imaging modality, which applies medium-frequency currents through skin-mounted electrodes and subsequent voltage measurements [1]. The acquired voltages undergo digital signal processing, enabling the reconstruction of the subject's conductivity distribution. EIT offers several advantages, including non-invasiveness, absence of radiation exposure, portability and high temporal resolution. However, its spatial resolution is limited due to the ill-conditioning and non-linearity of the occuring inverse problem. EIT is applied in diverse areas, including lung and cardiac monitoring [2], tumor detection [3], brain imaging and non-destructive evaluation.

The field of EIT imaging remains a focal point of research. Earlier approaches assumed a linear relationship between conductivity and electrode voltages, incorporating this concept into back-projection or Tikhonov regularization schemes [4]. Later, iterative non-linear Gauss-Newton (l_2-norm), total variation (l_1-norm) [5] and shape-driven methods were adopted. Recently, machine learning approaches have been introduced in EIT, including supervised neural network model-based [6], [7] and non-supervised ones [8]. Despite the improvements made in spatial, temporal resolution and robustness, major challenges remain in obtaining multidimensional structural and functional information efficiently.

This work combines a recently proposed point-matching method-of-moment (MoM) [9], [10], with a weighted block sparse Bayesian learning (WBSBL) approach [11] to perform 2-layer dynamic thoracic impedance imaging. The MoM formulates a system matrix using a Green integral equation, involving radial basis functions (RBFs) to express the logarithm of conductivity, reducing the problem's non-linearity and offering fast image reconstruction. At the same time, WBSBL assumes that conductivity perturbations are sparse and block contained in a number of clusters, with each one incorporating a self-trained hyperparameter [8], [12]. WBSBL is performed by exploiting structure aware priors and using the bound-optimization method with a weighted Gamma distribution prior [11]. It is characterized by improved stability and low sensitivity to noise. The proposed combination is evaluated on simulated human thoracic structures and real animal data, by stimulating 2 planes of a total of 32 electrodes. The resulting images sucessfully reveal the impedance changes due to the breathing process demonstrating significant artefact removal compared with the linear MoM approach.

The rest of this paper is organized as follows. Section 2 revises the MoM adopted, while section 3 describes the adaption of MoM to WBSBL, according to a 2-layer electrode scheme. In addition, section 4 describes the evaluation structures and presents the qualitative and quantitative results. Finally, section 5 draws the conclusion.

2. METHOD OF MOMENT

Assume a N-electrode EIT setup, tested within a n-dimensional domain Ω ($n = \{2, 3\}$) where the electrodes are located at the points $\{\boldsymbol{e_m}\}_1^N$ that lie very close to $\partial\Omega$. An electrostatic description of the EIT problem can be expressed from the following Poisson equation and Neumann boundary condition:

$$\nabla\big(\sigma(\boldsymbol{r})\nabla U(\boldsymbol{r};\boldsymbol{r}_+,\boldsymbol{r}_-)\big) = Ik\big(\delta(\boldsymbol{r}-\boldsymbol{r}_+)-\delta(\boldsymbol{r}-\boldsymbol{r}_-)\big), \quad (1)$$

$$U(\boldsymbol{r};\boldsymbol{r}_+,\boldsymbol{r}_-)\boldsymbol{v} = 0, \quad (2)$$

for any observation point $\boldsymbol{r} \in \Omega$. The current I is injected on the electrodes $\boldsymbol{r}_+, \boldsymbol{r}_- \in \{\boldsymbol{e_m}\}_1^N$, $\sigma(\boldsymbol{r})$ denotes the relative conductivity, U the voltage, $k = 1/m^n$ is a constant, δ the Dirac delta function and $\boldsymbol{v}$ is the normal outward-pointing vector. The Green function $G(\boldsymbol{r}, \boldsymbol{r'})$ is also defined:

$$\nabla^2 G(\boldsymbol{r}, \boldsymbol{r'}) = -\delta(\boldsymbol{r} - \boldsymbol{r'}), \quad \boldsymbol{r}, \boldsymbol{r'} \in \Omega \tag{3}$$

with the following boundary condition:

$$G(\boldsymbol{r}, \boldsymbol{r'})\boldsymbol{v} = -1/S, \quad \boldsymbol{r} \in \Omega, \, \boldsymbol{r'} \in \partial\Omega, \tag{4}$$

where S is the $\partial\Omega$ perimeter. Using (1)-(4) and the Green's second identity the following integral equation is derived [9]:

$$U(\boldsymbol{r}; \boldsymbol{r}_+, \boldsymbol{r}_-) = \int_\Omega G(\boldsymbol{r}, \boldsymbol{r'}) \nabla \left(\ln \sigma(\boldsymbol{r'})\right) \cdot \nabla U_o(\boldsymbol{r'}; \boldsymbol{r}_+, \boldsymbol{r}_-) dA + U_o(\boldsymbol{r}; \boldsymbol{r}_+, \boldsymbol{r}_-), \tag{5}$$

where U_o denotes the homogeneous case voltage. After the domain Ω discretization at L subdomains (pixels/voxels), $\ln \sigma(\boldsymbol{r'})$ can be expressed in a RBF manner:

$$\ln \sigma(\boldsymbol{r'}) = \ln(\sigma_o) + \sum_{j=1}^{L} c_j \exp\left(-\frac{\|\boldsymbol{r'} - \boldsymbol{r_j}\|_2^2}{2D^2}\right) \tag{6}$$

where $\{c_j\}_1^N$ are real constants and σ_o the background relative conductivity.

Substitution of (6) in (5) and discretization of the integral equation in a vectorized form, considering the current injection pattern and the voltage electrode measurements' sequencies, the following linear equation system is formed [9]:

$$\boldsymbol{M}\boldsymbol{c} = \tilde{\boldsymbol{U}}, \tag{7}$$

where $\boldsymbol{M} \in \mathbb{R}^{(Nh)\times L}$ is the system matrix, $\boldsymbol{c} \in \mathbb{R}^{L\times 1}$ the unknown coefficient vector and $\tilde{\boldsymbol{U}} \in \mathbb{R}^{(Nh)\times 1}$ the estimated electrode voltages (h is the number of voltage measurements obtained during the stimulation of a current electrode pair).

Assume the following noise model:

$$\boldsymbol{V} = \boldsymbol{M}\boldsymbol{c} + \boldsymbol{n}, \tag{8}$$

where $\boldsymbol{V} \in \mathbb{R}^{(Nh)\times 1}$ denotes the EIT system measurements vector and $\boldsymbol{n} \in \mathbb{R}^{(Nh)\times 1}$ the Gaussian measurement noise. Considering that the occuring inverse problem is ill-conditioned and in order to avoid overfitting, the following minimization scheme is defined:

$$\underset{\boldsymbol{c}\in\mathbb{R}^L}{\operatorname{argmin}} \Big\{ \|\boldsymbol{M}\boldsymbol{c} - \boldsymbol{V}\|_{\boldsymbol{W}}^2 + \alpha^2 R(\boldsymbol{c}) \Big\}, \tag{9}$$

where $\boldsymbol{V} \in \mathbb{R}^{(Nh)\times 1}$ denotes the EIT system measurements vector, $\boldsymbol{W} \in \mathbb{R}^{(Nh)\times(Nh)}$ a weighting covariance matrix, $R(\boldsymbol{c})$ a regularization term and α the regularization hyperparameter. The coefficients $\boldsymbol{c}$ can be estimated using a variety of l^1 and l^2-norm optimization algorithms, such as the generalized Tikhonov regularization (GTR) and the total variation (TV). Special attention should be given in the non-trivial process of the hyperparameter λ selection which strongly affects the result. The conductivity $\boldsymbol{\sigma} \in \mathbb{R}_+^{L\times 1}$ is estimated using (6).

Assuming a 2×16-electrode setup, with the electrodes located at $z = z_1$ and $z = z_2$ layers of the structure, the following system matrix is formulated as follows:

$$\tilde{\boldsymbol{M}} = \Big[\boldsymbol{M}|_{z=z_1} \boldsymbol{M}|_{z=z_2}\Big] \in \mathbb{R}^{(Nh)\times(L_1+L_2)}, \tag{10}$$

where $\boldsymbol{M}$ corresponds to a 3D case matrix and L_1, L_2 correspond to the number of pixels located within the 1st and the 2nd electrode layer respectively. Therefore, the problem (9) is reformulated with the modified matrix $\tilde{\boldsymbol{M}}$, thereby reducing the unknowns from L to $L_1 + L_2$, while maintaining the same number of measurements, Nh. The reconstruction is reduced on the electrode layers where the electric field is denser [13]. This mitigates the soft-field effect, thereby improving the ill-conditioning of the inverse problem. It is essential to note that the reconstruction problem is not handled separately for each layer, as their corresponding conductivity distribution is influenced by all of the electrode measurements.

3. WEIGHTED SPARSE BAYESIAN LEARNING

The SBL framework assumes that $\boldsymbol{c}$ in the model (8) is sparse, with each of the two layers consisting of $g_1 = L_1 - h_s + 1$ and $g_2 = L_2 - h_s + 1$ overlapping equally sized blocks (clusters) of $h_s > 1$ pixels. The minimization problem is modified as:

$$\underset{\boldsymbol{c}\in\mathbb{R}^{L_1+L_2}}{\operatorname{argmin}} \Big\{ \ln p(\boldsymbol{V}|\boldsymbol{c}) + \lambda \ln p(\boldsymbol{c}; \boldsymbol{\Theta}) \Big\}, \tag{11}$$

where $\boldsymbol{\Theta} = \{\lambda\} \cup \{\gamma_i, \boldsymbol{B_i}\}_{i=1}^{g_1+g_2}$ is a set of hyperparameters. In particular, $\gamma_i \in \mathbb{R}_+$ and $\boldsymbol{B_i} \in \mathbb{R}^{h_s\times h_s}$ quantify the i-th block's sparsity and intra-correlation structure respectively. To introduce the blocks' structure, $\boldsymbol{c}$ is factorized as $\boldsymbol{c} = \boldsymbol{\Psi}\boldsymbol{x}$:

$$\boldsymbol{\Psi} = [\boldsymbol{\Psi_1}, ..., \boldsymbol{\Psi_{g_1}}, ..., \boldsymbol{\Psi_{g_1+g_2}}] \in \mathbb{R}^{(L_1+L_2)\times(g_1+g_2)h_s} \tag{12}$$

with $\boldsymbol{\Psi_i} \in \mathbb{R}^{(L_1+L_2)\times h_s}$,

$$\boldsymbol{\Psi_i} = \begin{Bmatrix} [\mathbf{0}_{(i-1)\times h_s}^T, \boldsymbol{I}_{h_s\times h_s}, \mathbf{0}_{(L_1-i-h_s+1)\times h_s}^T]^T, \; i \le g_1 \\ [\mathbf{0}_{(i+h_s-2)\times h_s}^T, \boldsymbol{I}_{h_s\times h_s}, \mathbf{0}_{(L_1-i-2h_s+2)\times h_s}^T]^T, \; i > g_1 \end{Bmatrix},$$

$$\boldsymbol{x} = [\boldsymbol{x_1}^T, ..., \boldsymbol{x_{g_1}}^T, ..., \boldsymbol{x_{g_1+g_2}}^T]^T \in \mathbb{R}^{(g_1+g_2)h_s\times 1} \tag{13}$$

with $\boldsymbol{x_i} \in \mathbb{R}^{h_s\times 1}$ uncorrelated, $\boldsymbol{x} \sim \mathcal{N}(0, \boldsymbol{\Sigma_0})$ and $\boldsymbol{\Sigma_o} = \text{diag}\{\gamma_1 \boldsymbol{B_1}, ..., \gamma_{g_1+g_2} \boldsymbol{B_{g_1+g_2}}\} \in \mathbb{R}^{(g_1+g_2)h_s\times(g_1+g_2)h_s}$. The following matrices are also defined:

$$\boldsymbol{\Phi} = \tilde{\boldsymbol{M}}\boldsymbol{\Psi} \in \mathbb{R}^{(Nh)\times(g_1+g_2)h_s} \quad \text{and} \tag{14}$$

$$\boldsymbol{\Sigma_v} = \lambda \boldsymbol{I} + \boldsymbol{\Phi}\boldsymbol{\Sigma_o}\boldsymbol{\Phi}^{\boldsymbol{T}} \in \mathbb{R}^{(Nh)\times(Nh)}. \tag{15}$$

Therefore, the noise model (8) is written as:

$$\boldsymbol{V} = \boldsymbol{\Phi}\boldsymbol{x} + \boldsymbol{n}. \tag{16}$$

This work exploits the bound-optimization (BO) scheme, which is described by a surrogate convex function [14]:

$$G(\boldsymbol{x}, \boldsymbol{\gamma}) = \frac{1}{\lambda}\|\boldsymbol{\Phi}\boldsymbol{x} - \boldsymbol{V}\|_2^2 + \sum_{i=1}^{g_1+g_2} \text{Tr}\Big((\boldsymbol{\Sigma_v^*})^{-1}\boldsymbol{\Phi_i}\boldsymbol{B_i}\boldsymbol{\Phi_i^T}\Big)\gamma_i + \boldsymbol{x}^{\boldsymbol{T}}\boldsymbol{\Sigma_o}^{-1}\boldsymbol{x} + \ln|\boldsymbol{\Sigma_v^*}| - \sum_{i=1}^{g_1+g_2} \text{Tr}\Big((\boldsymbol{\Sigma_v^*})^{-1}\boldsymbol{\Phi_i}\boldsymbol{B_i}\boldsymbol{\Phi_i^T}\Big)\gamma_i^*, \tag{17}$$

where $\boldsymbol{\Phi_i} \in \mathbb{R}^{(Nh)\times h_s}$ denotes the submatrix of $\boldsymbol{\Phi}$ that corresponds to the i-th block. Furthermore, $\boldsymbol{\gamma}^*$ denotes a given γ-space point, with $\boldsymbol{\Sigma_v^*} = \boldsymbol{\Sigma_v}|_{\boldsymbol{\gamma}=\boldsymbol{\gamma}^*}$. The BO approach provides improved convergence rate compared with the expectation-minimization (EM) one.

Additionally to the BO SBL framework, a weighted prior is introduced, where each γ_i^{-1} obeys a Gamma distribution. The weights of each block, denoted as $w_i \in [0,1]$ and their corresponding inverses w_i^{-1} constitute the distribution's parameters. Therefore, according to the type-II maximum likelihood formulation, the objective function is written as:

$$H(\boldsymbol{x},\boldsymbol{\gamma}) = G(\boldsymbol{x},\boldsymbol{\gamma}) + 2\sum_{i=1}^{g_1+g_2}\frac{w_i}{\gamma_i} + 2\sum_{i=1}^{g_1+g_2}\frac{\ln(\gamma_i)}{w_i}. \quad (18)$$

The posterior mean values $\boldsymbol{\mu_x} \in \mathbb{R}^{(g_1+g_2)h_s\times 1}$ and covariance matrix $\boldsymbol{\Sigma_x} \in \mathbb{R}^{(g_1+g_2)h_s\times(g_1+g_2)h_s}$ of the blocks $\boldsymbol{x}$ can be estimated through an iterative minimization process of (18). Within each iteration their updates are given by:

$$\boldsymbol{\mu_x} = \boldsymbol{\Sigma_o}\boldsymbol{\Phi}^{\boldsymbol{T}}{\boldsymbol{\Sigma_v}}^{-1}\boldsymbol{V} \quad \text{and} \quad (19)$$

$$\boldsymbol{\Sigma_x} = \boldsymbol{\Sigma_o} - \boldsymbol{\Sigma_o}\boldsymbol{\Phi}^{\boldsymbol{T}}{\boldsymbol{\Sigma_v}}^{-1}\boldsymbol{\Phi}\boldsymbol{\Sigma_o}. \quad (20)$$

The learning rule for each hyperparameter is derived by differentiation of (18). In particular, the $\boldsymbol{\gamma}$ rule can be reduced to the inverse positive solution of a 2-nd order equation:

$$\gamma_i = \frac{A_i + 2w_i}{\frac{1}{w_i} + \sqrt{\frac{1}{w_i^2} + B_i(A+2w_i)}}, \quad (21)$$

where $A_i = \boldsymbol{\mu}_{\boldsymbol{x},\boldsymbol{i}}^{\boldsymbol{T}}{\boldsymbol{B_i}}^{-1}\boldsymbol{\mu}_{\boldsymbol{x},\boldsymbol{i}}$ and $B_i = \mathrm{Tr}\left((\boldsymbol{\Sigma_v^*})^{-1}\boldsymbol{\Phi_i}\boldsymbol{B_i}\boldsymbol{\Phi_i^T}\right)$. In addition, λ is updated through the following formula:

$$\lambda = \frac{1}{Nh}\left(\|\boldsymbol{V} - \boldsymbol{\Phi}\boldsymbol{\mu_x}\|_2^2 + \sum_{i=1}^{g_1+g_2}\mathrm{Tr}\left({\boldsymbol{\Sigma_x}}^{i}\boldsymbol{\Phi}_i^T\boldsymbol{\Phi}_i\right)\right). \quad (22)$$

The intra-block correlation matrix is updated by using an intermediate matrix:

$$\tilde{\boldsymbol{B}}_{\boldsymbol{i}}^{new} = \tilde{\boldsymbol{B}}_{\boldsymbol{i}} + \frac{1}{\gamma_i}\left(\boldsymbol{\Sigma}_{\boldsymbol{x},\boldsymbol{i}} + \boldsymbol{\mu}_{\boldsymbol{x},\boldsymbol{i}}\boldsymbol{\mu}_{\boldsymbol{x},\boldsymbol{i}}^{\boldsymbol{T}}\right). \quad (23)$$

in order to avoid overfitting. The updated $\boldsymbol{B_i}$ is given by

$$\boldsymbol{B_i}^{new} = \text{Toeplitz}\left([r_i^0, ..., r_i^{h-1}]\right), \quad (24)$$

$$\text{where} \qquad r_i = \text{sign}(\tilde{r}_i)\cdot\min\{|\tilde{r}_i|,\ 0.99\}, \quad (25)$$

$$\tilde{r}_i = \overline{\text{diag}\left(\tilde{\boldsymbol{B}}_{\boldsymbol{i}}, 1\right)}\Big/\overline{\text{diag}\left(\tilde{\boldsymbol{B}}_{\boldsymbol{i}}\right)}. \quad (26)$$

Finally, the weights are initialized by performing a single-step $\boldsymbol{c}$ estimation with NOSER l^2-norm prior according to MoM. Then each block's weight can be estimated by:

$$w_i = \frac{1}{h_s}\sum_{j=1}^{h_s}|c_j^i|, \quad (27)$$

where $\boldsymbol{c^i} \in \mathbb{R}^{h_s\times 1}$ denotes the i-th block's pixels' coefficient values. All the weights are normalized between 0 and 1. Fig. 1 depicts an example of the block structure and weight extraction at a pixelized thoracic single-layer domain.

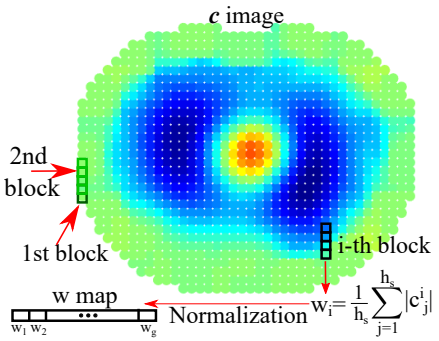

Fig. 1. Weight extraction from a block structured layer.

4. EVALUATION AND RESULTS

To evaluate the proposed approach, both simulated structures and real animal data have been used. In specific, 2 3D CT-based fine finite element (FE) adult male human thoracic structures have been generated using NETGEN and MATLAB software to simulate the electrode measurements. Each model has a height of 30cm and comprises approximately 1 million tetrahedral elements and 180000 nodes. The models incorporate lung cavities at full-inspiration (with a conductivity of 0.28S/m) and full-expiration (with a conductivity of 0.11S/m) breathing states, while the background conductivity was set at 0.36S/m. In addition, minor differences in chest and lung volumes between the 2 FE models were introduced to simulate dynamic behavior during the breathing process. The electrode layers were positioned at levels $z_1 = 12.8$cm and $z_2 = 17.3$cm, comprising a total of 2×16 electrodes. Furthermore, a square skip-4 current injection pattern was acted to intensify the electric field strength within the space between the electrode layers [15], [13]. Gaussian noise was also added to the measurements, resulting to a mean SNR of 50dB. A represtative case FE model is depicted in Fig. 2.

To avoid inverse crime [16], the 2-layer image reconstruction was performed at 2 coarse 1086-pixel sliced domains, exctracted from a 3D coarse voxelized structure at the electrodes' levels. Both single-step l^2-norm NOSER prior MoM and MoM-based WBSBL reconstructions were obtained ($\alpha = 4.5$, $D = 0.03$, $h_s = 4$, $\kappa_{\max} = 5$ iterations), with the corresponding time-difference EIT images shown in Fig. 3.

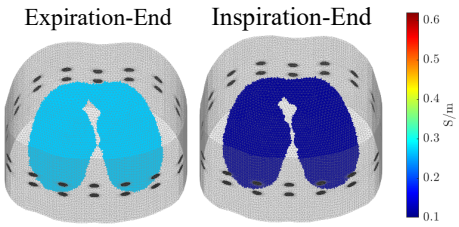

Fig. 2. Example of a 3D FE thoracic model. The electrode layers are also shown.

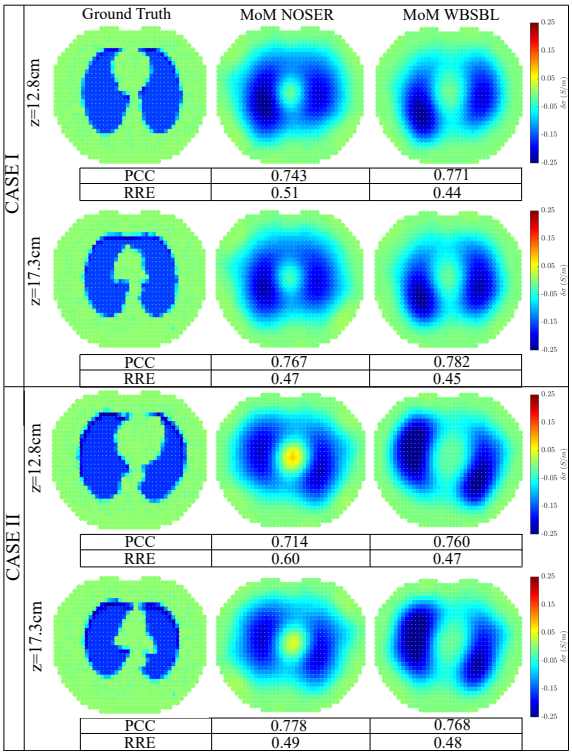

Fig. 3. Results of the 2 CT-based simulated thoracic cases.

An observation of the images shows that the MoM-WBSBL results demonstrate the breath-related conductivity changes more clearly compared to the single-step MoM l^2-norm one, with elimination of the artefacts. To quantitatively evaluate the images, the Pearson correlation coefficient (PCC) and the relative reconstruction error (RRE) metrics are considered for each layer separately, defined as:

$$PCC = \frac{\text{Cov}(\boldsymbol{\sigma}_{true}, \boldsymbol{\sigma}_*)}{\text{Std}(\boldsymbol{\sigma}_{true})\text{Std}(\boldsymbol{\sigma}_*)} \quad \text{and} \tag{28}$$

$$RRE = \|\boldsymbol{\sigma}_* - \boldsymbol{\sigma}_{true}\|_2 / \|\boldsymbol{\sigma}_{true}\|_2 \tag{29}$$

respectively. $\boldsymbol{\sigma_{true}}$ denotes the corresponding layer's ground truth and $\boldsymbol{\sigma}_*$ is the estimated $\boldsymbol{\sigma}$. The $\boldsymbol{\sigma_{true}}$ maps were obtained through an image registration process between the FE model and the pixelized slices. The PCC and RRE obtained for each case are also included in Fig. 3, demonstating an overall improvement in both metrics.

Finally, qualitative evaluation has been performed using real horse chest measurements at 2 electrode layers, online available in the EIDORS libary [17], [18]. For the reconstructions, 2 elliptic slices, each one comprised of 843 pixels, are utilized. Fig. 4 demonstrates half of a breathing cycle within 5 EIT imaging frames, where the air-flow impedance changes are detected from both MoM with NOSER and WBSBL approaches. However, MoM WBSBL eliminates major artefacts that could lead to misinterpretation of the images, providing clearer data for functional post-imaging analysis.

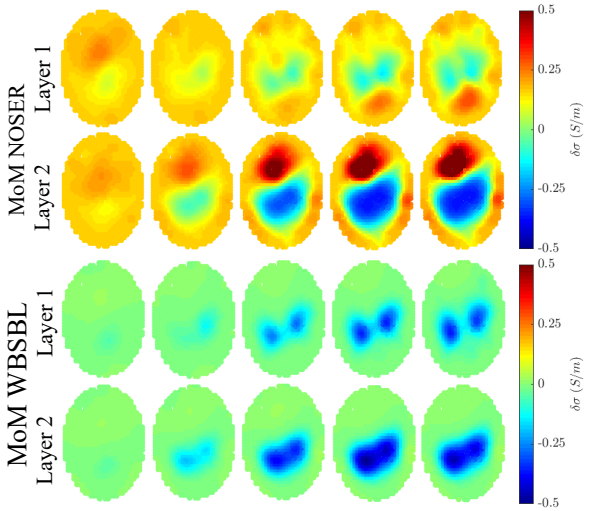

Fig. 4. EIT images based on horse lung data.

5. CONCLUSION

A 2-layer EIT reconstruction approach for lung monitoring is proposed. It combines an efficient point-matching MoM with a weighted prior SBL approach, which permits the self-training of the hyperparameters, while image artefacts are significantly reduced. Furthermore, z-axis structural and temporal information is acquired, avoiding the 3D case complexity. Further research should be conducted in complexity improvement and shape reconstruction enhancement.

Algorithm 1: MoM-based WBSBL for 2-layer EIT

Inputs: $\boldsymbol{V}$, D, α, h_s, ϵ_{min}, κ_{max}.
Initialize: $\epsilon = 1$, $\kappa = 0$, $\boldsymbol{\mu_x} = \mathbf{0}$, $\boldsymbol{\Sigma_x}$=$\mathbf{0}$, $\boldsymbol{\gamma} = \text{diag}\{\boldsymbol{I}_{(g_1+g_2)\times(g_1+g_2)}\}$, $\lambda = \sqrt{\frac{1}{Nh-1}\sum_{j=1}^{Nh}|V_j - \overline{\boldsymbol{V}}|^2}$, $\boldsymbol{B_i} = \text{Toeplitz}\left(\left[0.9^0, ..., 0.9^{h_s-1}\right]\right)$, $\boldsymbol{\Psi}$, $\boldsymbol{\Sigma_o} = \text{diag}\{\gamma_1 \boldsymbol{B_1}, ..., \gamma_{g_1+g_2}\boldsymbol{B_{g_1+g_2}}\}$, $\boldsymbol{\Phi} = \tilde{\boldsymbol{M}}\boldsymbol{\Psi}$, $\boldsymbol{\Sigma_v} = \lambda \boldsymbol{I} + \boldsymbol{\Phi}\boldsymbol{\Sigma_o}\boldsymbol{\Phi^T}$, $\tilde{\boldsymbol{B}}_{\boldsymbol{i}} = \boldsymbol{B_i}$.
Formulate the RBF in (6), $\boldsymbol{M}$ and $\tilde{\boldsymbol{M}}$ using MoM.
Estimate an initial $\boldsymbol{c}$ by minimizing (9) using $\tilde{\boldsymbol{M}}$.
Estimate $\boldsymbol{w}$ using (27) and normalize at $[0, 1]$.
While $\epsilon > \epsilon_{min}$ and $\kappa \leq \kappa_{max}$ **do**:
    Update $\boldsymbol{\mu_x}$ and $\boldsymbol{\Sigma_x}$ using (19), (20).
    Update λ using (22).
    For $i \in \{1, ..., g_1 + g_2\}$:
        Update γ_i using (21).
        Update $\boldsymbol{B_i}$ using (23)-(26).
        Update $\boldsymbol{\Sigma_o}$ and $\boldsymbol{\Sigma_v}$ using (15).
    $\epsilon = \|\boldsymbol{\mu_x}^{new} - \boldsymbol{\mu_x}^{prev}\|_2 / \|\boldsymbol{\mu_x}^{new}\|_2$, $\kappa += 1$.
Estimate $\boldsymbol{c_*} = \boldsymbol{\Psi}\boldsymbol{\mu_x}$ and $\boldsymbol{\sigma}_*$ using (6).

6. COMPLIANCE WITH ETHICAL STANDARDS

This research study was conducted retrospectively using animal subject data made available in open access by EIDORS. Ethical approval was not required as confirmed by the license attached with the open access data.

7. REFERENCES

[1] Andy Adler and David Holder, *Electrical impedance tomography: methods, history and applications*, CRC Press, 2021.

[2] Christian Putensen, Benjamin Hentze, Stefan Muenster, and Thomas Muders, "Electrical impedance tomography for cardio-pulmonary monitoring," *Journal of clinical medicine*, vol. 8, no. 8, pp. 1176, 2019.

[3] Juan Carlos Gómez-Cortés, José Javier Díaz-Carmona, José Alfredo Padilla-Medina, Alejandro Espinosa Calderon, Alejandro Israel Barranco Gutiérrez, Marcos Gutiérrez-López, and Juan Prado-Olivarez, "Electrical impedance tomography technical contributions for detection and 3d geometric localization of breast tumors: A systematic review," *Micromachines*, vol. 13, no. 4, pp. 496, 2022.

[4] Marko Vauhkonen, Dénes Vadász, Pasi A Karjalainen, Erkki Somersalo, and Jari P Kaipio, "Tikhonov regularization and prior information in electrical impedance tomography," *IEEE transactions on medical imaging*, vol. 17, no. 2, pp. 285–293, 1998.

[5] Andrea Borsic, Brad M Graham, Andy Adler, and William RB Lionheart, "Total variation regularization in electrical impedance tomography," 2007.

[6] Sarah Jane Hamilton and Andreas Hauptmann, "Deep D-bar: Real-time electrical impedance tomography imaging with deep neural networks," *IEEE transactions on medical imaging*, vol. 37, no. 10, pp. 2367–2377, 2018.

[7] Zichen Wang, Xinyu Zhang, Rong Fu, Di Wang, Xiaoyan Chen, and Huaxiang Wang, "Electrical Impedance Tomography Image Reconstruction with Attention-based Deep Convolutional Neural Network," *IEEE Transactions on Instrumentation and Measurement*, 2023.

[8] Shengheng Liu, Jiabin Jia, Yimin D Zhang, and Yunjie Yang, "Image reconstruction in electrical impedance tomography based on structure-aware sparse Bayesian learning," *IEEE transactions on medical imaging*, vol. 37, no. 9, pp. 2090–2102, 2018.

[9] Christos Dimas, Nikolaos Uzunoglu, and Paul P Sotiriadis, "An efficient point-matching method-of-moments for 2D and 3D electrical impedance tomography using radial basis functions," *IEEE Transactions on Biomedical Engineering*, vol. 69, no. 2, pp. 783–794, 2021.

[10] Christos Dimas, Vassilis Alimisis, Nikolaos Uzunoglu, and Paul P Sotiriadis, "A point-matching method of moment with sparse Bayesian learning applied and evaluated in dynamic lung electrical impedance tomography," *Bioengineering*, vol. 8, no. 12, pp. 191, 2021.

[11] Christos Dimas, Vassilis Alimisis, and Paul P Sotiriadis, "Electrical impedance tomography using a weighted bound-optimization block sparse Bayesian learning approach," in *2022 IEEE 22nd International Conference on Bioinformatics and Bioengineering (BIBE)*. IEEE, 2022, pp. 243–248.

[12] Shengheng Liu, Hancong Wu, Yongming Huang, Yunjie Yang, and Jiabin Jia, "Accelerated structure-aware sparse Bayesian learning for three-dimensional electrical impedance tomography," *IEEE transactions on industrial informatics*, vol. 15, no. 9, pp. 5033–5041, 2019.

[13] Bartłomiej Grychtol, Johannes Peter Schramel, Fabian Braun, Thomas Riedel, Ulrike Auer, Martina Mosing, Christina Braun, Andreas D Waldmann, Stephan H Böhm, and Andy Adler, "Thoracic EIT in 3D: experiences and recommendations," *Physiological measurement*, vol. 40, no. 7, pp. 074006, 2019.

[14] Zhilin Zhang and Bhaskar D Rao, "Extension of sbl algorithms for the recovery of block sparse signals with intra-block correlation," *IEEE Transactions on Signal Processing*, vol. 61, no. 8, pp. 2009–2015, 2013.

[15] Justin Wagenaar and Andy Adler, "Electrical impedance tomography in 3D using two electrode planes: characterization and evaluation," *Physiological measurement*, vol. 37, no. 6, pp. 922, 2016.

[16] William RB Lionheart, "EIT reconstruction algorithms: pitfalls, challenges and recent developments," *Physiological measurement*, vol. 25, no. 1, pp. 125, 2004.

[17] Andy Adler and William RB Lionheart, "Uses and abuses of EIDORS: an extensible software base for EIT," *Physiological measurement*, vol. 27, no. 5, pp. S25, 2006.

[18] Bartłomiej Grychtol, Johannes Peter Schramel, Ulrike Auer, Martina Mosing, Christina Braun, Andreas Waldmann, Stephan Böhm, and Andy Adler, "Focusing EIT reconstructions using two electrode planes," *ELECTRICAL IMPEDANCE TOMOGRAPHY!*, p. 17, 2017.